EXPERIMENTAL EVALUATION OF GLAUCONITIC SEDIMENTS FOR IN-SITU CARBON SEQUESTRATION

A THESIS
SUBMITTED TO THE FACULTY OF
UNIVERSITY OF MINNESOTA
BY

TIMOTHY J. KIESEL

IN PARTIAL FULFILLMENT OF THE REQUIREMENTS
FOR THE DEGREE OF MASTER OF SCIENCE

WILLIAM E. SEYFRIED JR.

APRIL 2018

Acknowledgements

I would first like to acknowledge my adviser Bill Seyfried for accepting me into the Department of Earth Sciences, for sharing his knowledge, experience, and time with an inexperienced student, and for his patience and motivation. I would also like to acknowledge the financial support and considerable laboratory space he provided for the work that allowed this thesis to be possible and the opportunity to work on an engaging project and gain invaluable experience. Special thanks go to Andrew Luhmann for his hours of invaluable instruction and expertise in experimental design and another special thank you goes to Ben Tutolo for hours of instruction and expertise in thermodynamics calculations. I wish to thank Chunyang Tan for designing and constructing experimental equipment and developing the associated control software. I thank Rick Knurr, Peter Solheid, Brian Bagley, Nick Seaton and Amy Myrbo collectively for the invaluable instrumental work that made this project possible, their expertise and the time they took to give me hands-on training. My sincere thanks go to my fellow lab mates Adam Schaen, for instructing me on the use of lab equipment and Drew Syverson, for always being available to discuss scientific concepts. I would like to acknowledge Sharon Kressler and Jennifer Petrie for helping me find my way through the paperwork to graduation. I would like to thank the faculties of the departments of Earth Sciences and at the University of Minnesota, especially my committee members Josh Feinberg and Dan Jones for their insightful comments and questions. I would also like to thank my parents Bill and Joanne for their love and support.

Abstract

Flow through experiments were conducted with intact glauconite-bearing Franconian Stage sandstone cores from the Tunnel City Group to determine the effectiveness of iron carbonate precipitation as a trapping mechanism for CO_2. In addition to quartz and glauconite, the rock contained small amounts of dolomite microspar. Mossbauer spectroscopy analysis indicated that the ratio of ferrous to ferric iron in the glauconite-bearing sandstone was 0.24. A key component of the experimental design entailed the use of a computer assisted fluid delivery system that permitted precise control of fluid flow rate (0.01 ml/min), as well as confining and pore fluid pressure (200 and 150 bar, respectively). Temperature was held constant at 150°C. The source fluid was a 1 molal NaCl brine charged with approximately 0.58 mol CO_2/kg solution. A second experiment was carried out to test the effect of imposed reducing conditions on the formation of iron carbonate minerals and phase relations involving glauconite. Permeability was continuously monitored and observed to decrease by approximately an order of magnitude for both experiments. The dissolved chemistry of outlet fluid provided evidence of fluid saturation with dolomite and siderite, while placing constraints on rates and processes of mass transfer. Potentiometric titrations performed on fluid samples revealed a decrease in alkalinity, consistent with the precipitation of carbonate minerals. This suggests that glauconitic sandstones may be a favorable host rock for carbon sequestration.

Table of Contents

List of Tables

List of Figures

Introduction

CO_2 is a ubiquitous product of human industry and emissions are expected to rise as a result of increased fossil fuel usage in developing economies. CO_2 tends to absorb near visible infrared radiation as part of its vibrational modes and then emitting the energy as thermal infrared radiation. This causes a warming effect on the atmosphere. Carbon dioxide is the second most abundant greenhouse gas in earth's atmosphere and can have a residence time of 1000 years (Solomon et al. 2009). The concentration of CO_2 has recently achieved a value of ~400ppm, well above the putative 280 ppm value that represents the putative pre-industrial concentration. Thus, further fossil fuel burning will have detrimental effects on global climate and the marine ecosystem. In order to reduce the effect of these emissions it has been proposed to capture carbon dioxide at a point source and then inject the CO_2 into deeply buried geological formations (DePaolo and Cole, 2013).

Storage may be accomplished by four different mechanisms: structural trapping, dissolution, capillary trapping and mineral formation (Kumar et al. 2005). Structural trapping is reliant on an impermeable layer of rock to limit the flow of water and supercritical CO_2 similar to a cap rock in petroleum reservoirs. Solubility trapping is achieved when the carbon dioxide is injected into the formation and dissolves into the subsurface fluids (Gilfillan et al. 2009). Dissolution of CO_2 into water causes hydrolysis of the compound to form carbonic acid which can lower the pH substantially. In the third method of sequestration, water contained in the pore spaces of sedimentary rock is displaced by CO_2 which then is held in place by increased capillary pressure (Pentland et

al. 2011). Water-rock reaction with carbonic acid can alter the permeability of the rock by dissolving minerals or closing up pore throats further trapping bubbles of CO_2. Mineral formation happens when cations present in the rock dissolve and react with carbonate species in the brine to form new solids. Carbonate minerals like dolomite can contain more than 40% carbon dioxide by weight. Mineralization can only account for a maximum of 18% of the CO_2 trapped. Accordingly, dissolution is typically the dominant trapping mechanism (Gilfillan et al. 2009).

Mineral trapping, however, is considered the most secure form of carbon sequestration because of its theoretically infinite residence time in CO_2 reservoirs (IPCC 2005). To better understand this process, several studies have been carried out on a variety of host rocks and minerals. Luquot et al. 2012 carried out an experiment in which CO_2 was percolated through chlorite and zeolite bearing sandstones. They reported the formation of ankerite, calcite and kaolinite from the dissolution of chamosite and laumontite. Similar experiments have been carried out on ferric sediments like banded iron formations. Sulphur dioxide was included in the experiment as a reducing agent and iron carbonates were formed as a result (Palandri et al 2009).

Xu et al. (2004) suggested glauconitic sandstones could be used as a host rock for carbon fixation and modeled long term water-rock reactions in a hypothetical reservoir. Their studies considered the use of simple organic acids and sulphur dioxide as reducing agents to better simulate the conditions found in oil basins and model time scales on the order of 100,000 years. Xu et al. (2004) model predicts that glauconite will react with CO_2 in coexisting brines, forming siderite from available ferrous iron. Models using

annite (an iron rich endmember of the biotite group) as a proxy for glauconite were run by other groups (Gunter et al. 1997), but this is not ideal because the simulations would not be representative of the kinetics and thermodynamics of glauconite dissolution. Currently CO_2 is being injected into the Utsira sand which contains Cenozoic glauconite (Pham et al. 2011). To test the reactivity of glauconite as a means of sequestering CO_2 as has been predicted by theoretical models, experiments were performed with glauconite-bearing sandstone and CO_2-bearing NaCl brine at temperatures and pressures broadly consistent with the modeled conditions.

Glauconite is a dioctahedral illite-like mineral that crystallizes in the monoclinic system and contains both ferrous (+2) and ferric iron (+3) (empirical formula: $K_{0.6}Na_{0.05}Fe^{3+}_{1.3}Mg_{0.4}Fe^{2+}_{0.2}Al_{0.3}Si_{3.8}O_{10}(OH)_2$) (Deer et al 1962). Dioctahedral refers to a structure where each octahedrally coordinated oxygen is surrounded by two cations. Glauconite is a mineral with interstratified smectite layers where the amount of smectite is inversely related to the potassium content (Odin 1988). Glauconite is usually associated with continental shelf sediments deposited during a transgression or rise in sea level (Chafetz and Reid 2000). Its origin is still largely unknown but it is thought to be related to the diagenetic alteration of sheet silicates by microorganisms and marine invertebrates, which create micro-reducing environments conducive to the formation of this clay. Glauconite is abundant in beds of Cambrian and Cretaceous age and is a widely distributed mineral. In North America it is present in the Flathead Formation in Montana, the Deadwood formation in South Dakota and the Tunnel City group found in Minnesota. Glauconite can appear as ooids, fibro-radiated rims on calcareous tests or in vesicles of

marine basalts (Tardy et al. 1987). When exposed to acid this mineral tends to release its divalent and monovalent cations into solution and form residual amorphous silica (Hassan and Baioumy 2006). Reaction of glauconite with CO_2 bearing brine can be expected to produce the minerals siderite and magnesite (Pham et al 2011).

In response to predictions based on computer models addressing glauconite reactivity in CO_2-bearing aqueous fluids, where secondary carbonate minerals are predicted to form in abundance, experiments were carried out at conditions broadly relevant to a number of carbon sequestration scenarios. For example, temperature and pressures for the experiments are in keeping with sequestration in deep sedimentary units where temperature and pressure can be quite elevated (Kharaka and Hanor, 2003). Accordingly, the temperature and pressure of the experiments was 150C and 200 bar, respectively. In contrast with static experiments, however, we employed a newly designed hydrothermal flow reactor with on-line sampling of the reaction fluid, which here was 1.0 mol/kg NaCl and 0.1 mol/kg $NaHCO_3$. Importantly, the experimental system permitted application of differential confining and pore pressure in keeping constraints imposed by natural systems. Alkalinity was included to buffer the pH of the sample to enhance the stability of carbonate minerals and has been used to enhance the carbonation of silicate minerals (Matter and Keleman 2008). One experiment was designed to test whether or not reducing conditions could enhance glauconite dissolution sufficiently to facilitate formation of siderite, as predicted form computed models. Reducing conditions were achieved by the addition of a redox buffer in the confinement fluid, which correspondingly imposed redox conditions in the Teflon core (see below)

containing glauconite-bearing reactants. In natural systems, reducing conditions are achieved in a less controlled way by the breakdown of organic matter coexisting with glauconite in the sedimentary units. The reaction fluid ($NaCl/NaHCO_3$) is far from equilibrium with respect to mineral reactants, facilitating mass transfer reactions, as might occur in the subsurface at a site close to where CO_2 is injected. It is important to emphasize that the glauconite-bearing sediment used for the experiments was cored from the source unit and not disaggregated subsequently. In fact, a critical aspect of the experimental design was to maintain the 3D rock geometry, while monitoring changes in permeability and fluid chemistry. Thus, the experiment will show how permeability of the rock evolves as the flow-through reaction proceeds and how mineral-fluid reaction rates change based on the amount of available surface area. The surface area normalized reaction rates were compared to values obtained from similar studies of glauconite dissolution kinetics.

Experimental Methods

Two experiments were carried out using the hydrothermal flow system to pass brine through the rock core sample at elevated pressure and temperature. Pressure was controlled by 4 ISCO Teledyne syringe pumps, while a stainless steel pressure vessel contained the rock core and confinement fluid, in effect permitting the desired operating pressure to be achieved. Pumps A and B were used to maintain flow constant at a rate of 0.01 mL/min, and provide pore fluid pressure (Figure 2). Pump C was used to provide confining pressure, while Pump D was used to maintain pressure at the outlet sufficient for fluid flow at the desired rate. In both experiments, pore fluid pressure was maintained

at 150 bar, while confining pressure was set at 200 bar. Confining pressure is always significantly higher than pore pressure to ensure that the experimental fluid flows through the rock core rather than around it. Inline pressure transducers record the pressure differential across the core for pre- and post-experiment permeability measurements. Permeability, k, was calculated using Darcy's law (Darcy 1865):

$$k = -\frac{Q\mu L}{A\Delta P} \quad (1)$$

where Q is volumetric flow rate, μ is fluid dynamic viscosity (950 μPa s at 22°C and 150 bar for deionized water reflecting the measurement, not the experimental, conditions) and was obtained from the NIST data tables, L is core sample length, A is cross-sectional area of the core, and ΔP is the pressure differential across the core. In practice, two titanium separators stored the acidic brine before and after circulation through the core. The titanium separators were necessary to prevent iron contamination from the stainless steel ISCO pumps during the experiment. The outlet fluid was sampled with a computer controlled valve that constantly released outlet fluid while maintaining constant pressure. Temperature was kept constant by four independently controlled band heaters attached to the confining vessel. The cores were contained in a Teflon sheath and PEEK retainer rings on both ends of the core. Metal foil was wrapped around the sheet to limit diffusion of CO_2 into the confinement vessel. The separators and the confinement vessel were purged with 5 bars of nitrogen prior to experiments to remove oxygen. The reactant brine was created by dissolving reagent grade NaCl and $NaHCO_3$ in deionized water (DI). CO_2 was added to the upstream separator resulting in a brine with a pH of approximately 5.7, which consisted of 1 molal NaCl, 0.1 molal $NaHCO_3$ and .57 mol/kg solution CO_2 (70%

of total saturation (Duan et al., 2006)). At the start of Experiment 2, DI water was passed through the core for 24 hours at 150°C before the experimental brine was released. To maintain reducing conditions as described above, iron filings in a Teflon container, were added to the DI water confining fluid external the Teflon sheathed, glauconite-bearing sandstone core. Thus, hydrolysis of the Fe˚ which occurred instantaneously at the experimental temperature provided dissolved H_2 that served as the reducing agent. Hydrogen, which diffused into the pore fluid in the Teflon flow reactor was measured by Gas Chromatography using a thermal conductivity detector. The concentration of CO_2 in both experiments was measured by attaching a gas tight syringe at the outlet and using the volume of gas and the mass of fluid, hereafter referred to as the manometric technique (Luhmann et al. 2013). Inductively coupled plasma–optical emission spectrometer (ICP-OES) was used to analyze the oxide composition of the whole rock and the glauconite (Tables 1 and 2). Normalizing the ICP-OES data for glauconite to a 10 $O(OH)_2$/unit cell gives a composition of $Na_{0.19}Ca_{0.03}K_{0.62}Fe(III)_{1.05}Mg_{0.3}Fe(II)_{0.08}Al_{0.62}Si_{3.9}O_{10}(OH)_2$. Mineral abundances in the whole rock were determined by taking the values from ICP-OES and assuming all iron could be attributed to glauconite. Then the ratio of iron to potassium was used to determine how much of that element could be attributed to glauconite. The residual potassium was used to set the abundance of k-feldspar. Once those had been established the silica from glauconite and K-feldspar was subtracted from the total to determine the amount of quartz in the core. Dolomite was set equal to calcium. The relative abundances were normalized to a hypothetical 5g rock core and

then totaled. A Rigaku Miniflex benchtop x-ray diffraction instrument (XRD) was used to verify the presence of glauconite, quartz and dolomite.

Mossbauer Spectroscopy was used to determine the ferrous to ferric ratio of the iron in the glauconite and the cores post reaction. The Mossbauer Effect is the resonant recoilless absorption of gamma rays by the nuclei of certain elements (Dyar 2005). The gamma source in this case was Co-57 which interacts with the Fe-57 present in the sample. It is assumed the oxidation state ratio of this isotope is representative of all of the iron. This techniques can measure the ferrous/ferric ratio because the differing electron orbitals in the ions have different "screening" effects creating two distinguishable "doublets" of absorption at the measured energy levels. ICP-OES was also used to measure the concentration of cations in the outlet fluid. 2σ error was 2% of the reported concentrations. Prior to analysis, fluid samples were passed through a 2 micron filter to ensure that the fluid did not contain any particulate solids, and acidified with trace metal grade HCl to prevent the formation of any secondary minerals during storage. Alkalinity was measured by titrating the samples to the bicarbonate endpoint with an acid of a known normality (Gran 1950).

Following the experiments, the pressure vessel was quenched rapidly to prevent mineral precipitation in response to cooling effects. Valves to the separators were closed and bypass lines were opened to pump DI water through the core to flush residual brine from the pore space. Once removed from the reactor, the cores were dried at 60°C for a day and weighed to determine mass change based on comparison with earlier recorded pre-experiment data of this sort. The mass of the wet and dry cores post-reaction, were used

to estimate the bulk porosity for the core. Full-core X-ray Computed Tomography (XRCT) imaging was performed pre- and post-experiment at 8 μm voxel size at the University of Minnesota XRCT laboratory. At this resolution it can characterize any dissolution/precipitation, changes in pore geometries and grain reorganization. Geometric surface area was estimated by obtaining the median grain side of the rock through sieve analysis which is proportional to the geometric modeled as uniform spheres (White and Peterson 1990).

Distribution of aqueous species calculations used throughout to interpret phase equilibria and kinetics were conducted using Geochemist's Workbench (GWB, Bethke and Yeakel, 2012) version 9.0.9 with the SUPCRT92 data set (Helgeson et al. 1978; Johnson et al. 1992; Sverjensky et al. 1997) that was modified to reflect conditions at 150°C and 200 bar by the program DBCreate (Kong et al. 2012)..In all relevant speciation and thermodynamic calculations, thermodynamic data for Al-bearing minerals were obtained from the thermodynamic data set presented by Tutolo et al. (2014). Other mineral and aqueous species thermodynamic properties are taken However, revised thermodynamic properties of Al aqueous species and H_4SiO_4(aq) were obtained from the revised thermodynamic data sets of Tagirov and Schott (2001) and Stefansson (2001), respectively. Saturation index (Ω) was calculated according to:

$$\Omega = \log(\frac{Q}{K}) \quad (2)$$

where Q is the ion activity product and K is the equilibrium constant.

As emphasized throughout, an important objective of the research was to evaluate the reactivity of glauconite in aqueous CO_2 bearing NaCl fluids and determine whether or

not mass transfer reactions involving glauconite could account for formation of Mg and Fe bearing carbonate minerals. Glauconite, not being a common mineral, however, is underrepresented with respect to thermodynamic data, and thus, to accomplish the stated objective it was first necessary regress data for this mineral using a combination of estimation techniques. In the present study, we estimated the thermodynamic properties of glauconite at 25C and 1 bar assuming a composition broadly consistent with that determined here, while using the algorithm outlined by Tardy et al (1987) and thermodynamic data (see above) for requisite aqueous species involved in glauconite hydrolysis equilibria. These data, coupled with temperature dependent thermodynamic data for an appropriate series of reference reaction allowed determination of molar volume, entropy, and heat capacity of glauconite at experimental conditions (150C, 200 bars) (Appendix 1).

Results and Discussion

The two experiments we present in this study were designed to investigate the fate of glauconite and associated minerals when reacted with CO_2-bearing NaCl brine at conditions relevant to sequestration of CO_2 in deep seated sedimentary formations. Importantly, the experiments were explicitly designed to test the role of redox on the relative stability of glauconite, in an attempt to simulate the more complex redox processes associated with organic geochemical reactions in natural systems at elevated temperatures and pressures. Thus, experiment 1 simply entailed reaction with CO_2-bearing NaCl, while experiment 2 was similar in every way except for the moderately elevated dissolved H_2 concentrations that served as redox buffer.

3.1 Fluid chemistry and saturation states

Fluid samples taken from the outlet in experiments 1 and 2 show an initially large release of cations from constituent minerals upon exposure of the core to the experimental fluid, and a subsequent decrease and approach to a steady state, which is then maintained for the length of the experiment (Fig. 4). Aluminum and silica bearing species are an exception to this pattern owing to the tendency of these components to form secondary minerals. Dissolution reactions tend to preferentially occur at certain high energy sites on the mineral surface related to crystal defects (e.g., Helgeson et al., 1984; Lasaga et al., 1998). This pattern suggests that there is an initial high availability of reactive sites in the rock that is depleted over the length of the experiment. Furthermore, surface area of the primary minerals is also likely gradually diminished by the precipitation of secondary Al-bearing minerals, as evidenced by the relative lack of Al in the fluid samples.

Saturation indices calculated from the fluid samples illustrate that the system is always supersaturated with respect to kaolinite and boehmite, consistent with the low solubility of Al (Fig. 5). In the case of dissolved Si, the steady state concentration is likely best explained by constraints imposed by quartz solubility, particularly when considering the abundant presence of quartz throughout the core as well as the fact that all samples are at or near quartz saturation (Fig. 5 and 6). Several experiments performed with a NaCl CO^2 brine on various mineral assemblages show this solubility limitation on illite clays (Kaszuba et al 2005), feldspar with quartz (Tutolo et al. 2015), K-feldspar alone (Lu et al. 2013). Experiments on a chlorite-rich sandstone (Luquot et al. 2012)

found that dissolved silica was slightly oversaturated with respect to quartz. Although Fe is always at or near detection limits, data that are available suggest saturation with respect to siderite. In both experiments, fluid samples are initially near K-feldspar saturation, but soon become undersaturated with reaction progress. In contrast, fluid samples are initially highly supersaturated with respect to dolomite, and gradually trend toward saturation as the experiments proceed (Fig. 5). Fluids from both experiments indicate undersaturation with respect to glauconite (Ω always<-2) according to the thermodynamic values estimated in Appendix 1. This is consistent with the extreme reactivity of glauconite seen in the micrographs taken of the upstream section of both cores. In this model the fugacity of oxygen is set to be in equilibrium with hematite. Not surprisingly, the dissolved concentration of Fe is higher in experiment 2 than 1 due to the reducing agent (Table 5 and 6) (Hem 1960; Tremaine and LeBlanc 1980; Jensen et al. 2002), but still lower than for similar experiments involving arkose sandstone (Tutolo et al 2015). The arkose experiments, however, were conducted with fluids having relatively low alkalinity and correspondingly lower pH, which might account for the relatively high dissolved Fe. The concentration of iron strongly tracks the concentration of molecular hydrogen in the fluid suggesting that The most apparent difference in fluid chemistry is the steady state value for K^+ is 600 μmol/kg greater and there are 5 more meq/kg alkalinity removed from solution in experiment 2 than experiment 1 (Table 5 and 6). This suggests greater reactivity of the brine with glauconite under the reducing conditions of the second experiment. Also dissolved magnesium reaches the steady state value mush faster during experiment 2 (Figure 5). The dissolution of glauconite in CO_2 bearing

aqueous fluid is expressed according to the reaction depicted in (equation 4 and 5). Iron and aluminum species are conserved owing to the formation of secondary minerals such as goethite and kaolinite, respectively. Experiments done on glauconite with batch reactors at similar temperatures and pH close to 3.5 recorded concentrations of 25 mmol/kg, two and a half times the maxima of our experiments further suggesting that the brine is always far from equilibrium (Sass et al. 2001; Gunter et al. 1997).

3.2 Element mobility and mass balance

Stepwise integration of the fluid chemistry compared with elemental abundances in the rock core shows the relative mobility of different elements within the rock according to the equation (Luhmann et al. 2014):

$$Element\ recovery(wt\%) = \frac{M_i Q_m \int_{t'=0}^{t'=t} \Delta C_i(t')dt'}{m_{core} F_i} x\ 100 \quad (3)$$

where M_i is the molecular mass of element i, Q_m is the discharge rate, ΔC_i is the outlet concentration of element i, m_{core} is the mass of the core, and F_i is the element weight fraction in the core

Calcium is the most mobile species in both experiments (Table 8 and 9). Calcium is preferentially being removed from the core, which suggests that the carbonate cement is being preferentially dissolved. ICP-OES analysis shows that the rock contains more moles of magnesium than it does calcium (Table 2). Because magnesium is more abundant in the rock it is expected that the total extraction percentage of magnesium would be less than calcium, however the comparison of extraction profiles is complicated by the presence of other calcium phases like apatite. The ratio of calcium to magnesium

suggests that the fluid is not controlled entirely by the dissolution of dolomite. The brine is always oversaturated or saturated with respect to carbonates especially dolomite which is expected because there is a kinetic barrier to precipitation. Both experiments removed approximately 2% of the rock but only 0.85% of the available silicon further indicating that silica was limited to equilibrium solubility. During experiment 2 it is apparent that there was more potassium mobilized relative to calcium than in experiment 1 (Table 9). There was also less magnesium mobilized relative to the calcium compared to experiment 1 suggesting that a secondary magnesium phase formed during experiment 2 or the magnesium in glauconite was less mobile. The absolute magnitudes of element mobility were significantly different between the two experiments (for example 15 wt% Ca mobilized during experiment vs. 10 wt% during experiment 2) but this is believed to be related to flowing 150°C DI water through the core for 24 hours at the start of experiment 2, potentially consuming reactive sites and affecting the sample collection schedule, and not the addition of a reducing agent.

3.3 Alkalinity

Importantly total alkalinity was measured as decreasing from 92 meq/kg to 82 meq/kg during experiment 1 and showed a removal of 15 meq/kg from the brine in experiment 2. Alkalinity in meq is defined as the equivalent number of moles of 1 normal acid the solution could neutralize. The incongruent dissolution of silicates typically increases the alkalinity of Na-HCO_3-CO_2 solutions through the consumption of H^+ and the mobilization of cations that are charged balanced by bicarbonate anions (e.g., Garrels 1965). This effect has been seen in numerous carbon sequestration experiments however

most of them do not include a brine that has already been buffered with bicarbonate (Sass et al. 2001; Gunter et al. 1997; Kazuba et al. 2005; Tutolo et al. 2015). Alkalinity can be reduced by the precipitation of minerals but monovalent cations like K^+ are extremely soluble at experimental conditions so a silicate buffering model would still predict an increase in alkalinity (e.g., Garrels and McKenzie 1967). We therefore hypothesize that, due to the high concentration of Na^+ in the inlet solution, the alkalinity is being reduced in these experiments by a replacement reaction similar to:

$$1\ K_{0.6}Mg_{0.25}Al_{1.8}Al_{0.5}Si_{3.5}O10(OH)_2\ (\text{illite}) + 0.3\ Fe_3O_4 + 0.04\ H_2O + 1.6\ Na^+ + 0.25\ HCO_3^- + 0.08\ O_2 = 0.6\ K^+ + 0.65\ AlO(OH) + 0.25\ MgCO_3 + 0.9\ FeO(OH) + 1.7\ Na_{0.96}Al_{0.96}Si_{2.04}O_6\ (\text{analcime}) + 0.78\ H^+ \quad (4)$$

$$1\ K_{0.6}Mg_{0.25}Al_{1.8}Al_{0.5}Si_{3.5}O10(OH)_2\ (\text{illite}) + 0.3\ Fe_3O_4 + 1.6\ Na^+ + 0.15\ H^+ + 1.15\ HCO_3^- + 0.3\ H_2 = 0.6\ K^+ + 0.65\ AlO(OH) + 0.25\ MgCO_3 + 0.9\ FeCO_3 + 1.7\ Na_{0.96}Al_{0.96}Si_{2.04}O_6\ (\text{analcime}) + 1.63\ H_2O \quad (5)$$

At a pH of 5.7 precipitation of carbonate minerals can also be a source of acidity. This reaction is analogous to processes observed during injection of 300°C saline water into a sedimentary basin for oil recovery (Hutcheson and Abercrombie 1990). Instead of H^+, sodium is exchanged for the soluble cations in the mineral and acidity is produced by the formation of secondary phases (Hutcheson et al. 1993). In this schematic reaction illite is used as a proxy for glauconite and magnetite is added to model the presence of ferrous and ferric iron in the mineral. Equation 4 reflects experiment 1 where there is residual dissolved oxygen that reacts with iron to form a ferric phase while equation 5 shows the effect of dissolved hydrogen. Analcime is not predicted or observed to form but is a proxy for sodium silicates like montmorillonite that might be an alteration product of glauconite. Interestingly analcime was observed to precipitate in other carbon

sequestration experiments on illite at 200 C with a 5M NaCl brine (Kazuba et al. 2005). This schematic reaction is consistent with several observations of the fluid chemistry in addition to the consumption of alkalinity: the conservation of aluminum and iron as solid phases and the lower mobility of magnesium into solution by the potential precipitation as magnesite. Since dissolved magnesium and iron are exchange products for sodium in these proposed reactions and there was greater retention of magnesium during experiment 2, the greater magnitude of alkalinity removal is suggestive of greater precipitation of carbonates. The apparent decrease in Na^+ in the outlet fluid is close to the measurement error so it is difficult to quantify how much is being removed. Previous studies of carbon sequestration using glauconite in batch reaction experiments noted that the mineral did take up excess sodium while interacting with a CO_2 brine but this experiment was run at a lower pH (Sass et al. 2001).

3.4 Dissolution kinetics

Rates of mineral dissolution have been shown to be a complex function of solution pH, temperature, and secondary mineral precipitation rate. The temperature and pH dependence of a first order mineral dissolution reaction is commonly modeled using a simplified form of the general transition-state-theory (TST) derived rate law as given by (Lasaga 1984; Helgeson et al. 1982; Hellevang et al 2013; Pham et al. 2011):

$$r = k \prod aH^{+v} e^{\left(-\frac{Ea}{RT}\right)} (1 - \Omega) \quad (6)$$

where r is the reaction rate in units of mol/m^2/s, k is the rate coefficient, aH^+ is the activity of hydrogen ion in solution, v is the reaction order with respect to hydrogen ion, Ea is the activation energy for the dissolution reaction in kJ/mol, R is the molar gas

constant, T is the temperature in Kelvin and Ω is the saturation state of the mineral of interest in the fluid. Calculations discussed above indicate that Ω << 1 for the glauconite dissolution reaction, which allows for saturation state dependence in Eqn. 6 to be ignored here. Aagaard et al. (2004) determined from experiments performed in mixed flow reactors that the apparent activation energy of the glauconite dissolution reaction at pH 2 is ~35 kJ/ mol, the apparent reaction order with respect to H^+ is –0.28 and the rate constant for glauconite is 4.788×10^{-10} mol/m^2/s at 37 °C. This model predicts that the reaction rate at the experimental conditions of 150°C and a pH of 5.7 will be $8.3x10^{-13}$ mol/m^2/s.

The bulk reaction rate, *r*, in units of mol/m^2/s for the dissolution of a mineral in a hydrothermal flow-reactor may be calculated according to equations the following reaction (Dove and Crerar, 1990; Hellmann, 1994; Tutolo et al., 2014b, 2015)

$$r = \frac{\Delta C \cdot Q}{(S \cdot A)} \quad (7)$$

ΔC is equal to the measured change in concentration in mol/kg sol. of the element of interest. *Q* is the flow rate of the system in kg/s. *S* is the stoichiometric number of the element in the crystal structure of glauconite. *A* is the estimated BET surface area in m^2/g of rock multiplied by the mass of the glauconite as determined by the ICP-OES. Previous studies report the BET surface area is 0.0178 m^2/g for glauconite (Pham et al. 2011).

Dissolution rates are high in the early stages of both experiments and then decrease as the experiment proceeds. The steady state reaction rate for experiment 1 was calculated as $5.8x10^{-9}$ mol K^+/m^2/s using equation 1 assuming 0.6 mol K per mole of glauconite. The brine theoretically contains only sodium cations, so it is far from

equilibrium for the minerals in the experimental core. Since potassium is an extremely mobile element and doesn't form a secondary phase it can be used as a proxy for the reaction of glauconite. Interestingly, the bulk rate is calculated as being four orders of magnitude faster than the one derived from transition state theory. There is a recognized discrepancy in the rate constants between different laboratories and the reaction rate between laboratory and field values (White and Brantley, 2003). It should be noted that the same BET surface area for glauconite, which was not actually measured on our samples, was used in all calculations. In the case of these experiments, part of the discrepancy might be due to the high ionic strength of the brine.

The rate of glauconite dissolution is extremely important to the process of carbon sequestration because silicates react much more slowly than carbonates (Brantley 2008; Dove and Crerar 1990; Golubev et al. 2009; Pokrovsky et al. 2009; Saldi et al. 2009; Yang and Steefel 2008). Since glauconite is a source for divalent cations to form new carbonates, dissolution is a rate limiting step in the carbonation process. Glauconite can tolerate a high degree of dissolved cations and still stay far from saturation so it is not likely that dissolution kinetics are controlled by the formation of secondary minerals unlike feldspars where Al concentrations have a greater effect on the saturation state (Alekseyev et al. 1997). The steady state concentration of potassium was 1.08 mmol/kg in experiment 2 versus 0.8 mmol/kg in experiment 1, suggesting that the reaction of the brine with glauconite proceeds faster under reducing conditions.

3.5 Textural and redox changes to minerals in the core

Reaction of glauconite is characterized by textural changes that are best illustrated by the development of a honeycomb-like texture (Figure 7). The surface of the grain is often referred to as the cortex in literature and its alteration is qualitative evidence of the reactivity of glauconite during the experiments (Odin 1988). In experiment 1, the alteration is accompanied by the formation of a botryoidal-shaped phase, which based on EDS determined the iron oxide mineral being precipitated had an oxygen to iron ratio of 2:1 of suggesting the secondary phase was goethite (Figure 11). Analysis of different regions of the core from fluid inlet to outlet indicate that it is the former region that reveals the greatest evidence of reaction and mass transfer between solids and the fluid. K-feldspar provides the best evidence of this where obvious dissolution features up-core are superseded down core by a mineral (K-feldspar) that shows virtually no effects of dissolution (Figure 9). Fine grained lamellar aluminum minerals were found to be precipitating on quartz grains (Fig. 8). Minerals with a similar morphology were characterized as boehmite in a previous study run at similar conditions (Fu et al. 2009). It is secondary minerals such as these that armor the surface area of grains from reaction with the brine and block up pore throats decreasing the permeability of the rock.

The behavior of redox-sensitive components within this experimental system is one of the central concerns of this study. Redox effects can be difficult to study in rock-water interactions because solutions are often found to be out of redox equilibrium at low temperatures (Lindburg and Runnels 1984; Seewald 1994). However, with modern instrumental methods such as Mossbauer spectroscopy, it is possible to characterize the oxidation state of iron phases present in representative rock samples before and after the

experiments. Otake et al. (2007) determined that mixed ferrous-ferric minerals like magnetite could be hydrothermally transformed to ferric minerals like hematite even in the presence of aqueous hydrogen, suggesting that at 150°C reaction between iron minerals and a reducing agent will not be kinetically favorable. However Foustoukos et al. (2011) showed that even at 150°C hydrogen can rapidly react with and decrease the fugacity of oxygen. Mossbauer spectroscopy is not typically used to identify minerals but different minerals can have characteristic isomer shifts and quadrupole splitting ranges that can aid discrimination in a mixed sample (Dyar et al. 2006). 2 sigma error for isomer shift and quadrupole splitting is 0.02 mm/s (Dyar et al. 2007). Mossbauer spectra collected for glauconite have distinguishable doublets created by the octahedral coordinated ferric and ferrous iron. Siderite has a diagnostic isomer shift of 1.2 and quadrupole splitting of 1.8 (Dyar et al. 2006). The spectra collected from the unreacted rock indicates that there is both glauconite and siderite present (Table 3). The samples for experiment 1 and 2 were taken from the most upstream region where the reaction was expected to be the most aggressive. The dissolution of glauconite is a redox sensitive process (Xu et al. 2004) and according to our thermodynamic model glauconite is predicted to be oversaturated with respect to the fluid in the presence of even micro molar concentrations of oxygen.

During experiment 1, an attempt was made to sparge all oxygen from the experimental fluids using nitrogen gas. If completely effective, this procedure should have left a theoretical residual oxygen concentration of 6 μmol/kg (Butler et al. 1994). Alteration of the rock by the brine induced the formation of botryoidal ferric oxides on

the upstream endcap. Mossbauer shows alteration of the rock during experiment 1 decreased in the ratio of ferrous to ferric iron from 0.24 to 0.22 (Table 7) in the upstream region suggesting that the residual oxygen reacted with the present ferrous minerals (Fanning et al. 1989; Duckworth and Martin 2004). Magnetically ordered minerals were beneath the detection limit of the instrument. The change indicates that sparged experimental fluid was too oxidizing for the siderite to be stable initially but the fluid chemistry shows the core reaches a new equilibrium when oxygen is consumed by the precipitation of the new ferric phase. Dissolved potassium from the fluid chemistry and SEM images show that glauconite was reactive during experiment 1, which is consistent with our thermodynamic model where the activity of molecular oxygen is set in equilibrium with a ferric phase. The concentration of dissolved iron was supersaturated with respect to siderite, which suggests that goethite and siderite can coexist after the consumption of molecular oxygen. However it is the ferrous iron itself which regulates the activity of oxygen which means that any Fe^{2+} dissolved from glauconite will be unavailable to react with carbonate and with no redox controls these results suggest a net decrease in the amount of siderite in the rock or no change at all. The formation of goethite and the change in bulk oxidation state of the rock during experiment 1 suggests that glauconite is not an ideal host rock for carbon sequestration if there are no available organic compounds in the reservoir to consume residual oxygen and create a reducing environment. Siderite was not likely a net sink for CO_2 in experiment but it is still possible that dissolved magnesium was able to contribute to carbonate mineralization.

Oxidation of zero-valent iron particles in the confining vessel was used to generate hydrogen to act as a reducing agent during experiment 2. A Teflon sheath is used to separate the fluids of the confining vessel but this sheath is permeable to gases which means the concentration of CO_2 and hydrogen was the same in the confining vessel and the experimental core. XRD and SEM-EDS analysis of the iron post-experiment shows that the iron metal was converted entirely to siderite. Since the conditions in the confining vessel are the same as the experimental core the formation of siderite suggests that it is thermodynamically possible to convert iron components in the core to siderite (Barnes and Clarke 1969). When the values for CO_2 and hydrogen were plotted on an activity diagram siderite was consistently the most thermodynamically favorable iron mineral for the length of the experiment (Fig. 3). Saturation indices calculated in GWB from dissolved cations similarly indicated fluid super saturation with respect to siderite. Mossbauer spectroscopy of the reacted rock from experiment 2 shows the ratio of ferrous to ferric iron in the sample is 0.34 compared to the unreacted rock which has a ratio of 0.24 (Table 7) along with an increase in the area of the doublet associated with siderite and a decrease in the area of the doublet associated with the ferric iron in glauconite. This is consistent with the dissolved molecular hydrogen reducing the structural ferric iron which enhances the dissolution of glauconite and the dissolved iron subsequently reacting with bicarbonate to form siderite. An increase in the amount of ferrous iron coupled with the favorable thermodynamic environment suggests that there was carbonate mineralization created from a net gain in siderite. Analysis of several regions in the core

for both experiments suggest that compositional heterogeneities in the rock cannot account for the differences in ferrous to ferric ratio found in the two experiments.

3.6 Physical changes

Following early stage instability, the pressure differential for fluid flow at a flow rate of 0.01 ml/min during experiment 1 achieved sufficient stability such that the permeability could be determined using Darcy's Law (Fig. 10). The gradually increasing Δ P determined from the difference in inlet and outlet fluid pressure during fluid flow (0.01 ml/min) suggests a permeability decrease. This decrease is likely caused by the precipitation of sheeted or lath-shaped minerals such as boehmite, kaolinite and montmorillonite (Cerda 1987). These fine grained clays can block off pore throats and form on mineral surfaces. During the second experiment permeability decreased by an order of magnitude. XRCT shows that the rock is composed of coarse grained sediments with large easily distinguishable pore spaces which along with the extreme initial permeability suggests that they are highly interconnected and have a high degree of access to mineral surface area. The images show that a cavity formed in the inlet portion of the core during experiment 1 from dissolution and grain reorganization and compaction of the core against the PEEK endcaps (Fig. 10). No cavity was observed in the core from experiment 2. The rock was extremely friable after interaction with the brine, which is consistent with the dissolution of cement. The core mass decreased by approximately 2% in each experiment (Table 1). The similar measured changes in mass between the two experiments suggests that approximately the same amount of dissolution and precipitation occurred in all experiments in spite of their different redox conditions.

The change in mass and the increased friability of the rock suggests that porosity is increasing due to the dissolution of carbonate cements but there is still a measurable decrease in permeability and reactive surface area as mentioned before. The rates of primary mineral dissolution or decrease in concentration of cations in both experiments that any additional surface area created by grain-scale dissolution or etching of the mineral is reduced by the precipitation of secondary minerals. Despite potential porosity increases in some areas of the core localized incidents of mineral precipitation, porosity decrease plugging of pore throats can decrease the permeability of the whole core. This is because the bulk permeability of materials in series is dominated by the lowest permeability layer (Alexander and Saar, 2012; Tutolo et al. 2015). Despite measurable decreases in the cores during both experiments they remain highly permeable in an absolute sense suggesting that glauconite alteration will not diminish the suitability of a reservoir to transmit CO_2 charged brines.

3.6 Comparison to extant models

Some geochemical models dispute the ability of glauconite to sequester carbon dioxide. Fu et al. (2015) suggests that glauconite is stable at slightly oxic conditions similar to experiment 1 of this study and that glauconite is unstable under reducing conditions but tends to form secondary minerals like berthierine which sequester iron and magnesium making them unavailable to form carbonates. This is based on examination of the Siri oilfield which contains rock with glauconite and berthierine. The geochemical data that was estimated for glauconite in this study supports this and predicts that glauconite is over saturated in the presence of even small amounts of oxygen. However

the characteristic dissolution rate of potassium and the textural changes shown in the SEM suggest that glauconite is reactive in both suboxic and reducing CO_2 charged brines. This contradiction might be explained by the differing compositions found in the Siri oilfield versus the Tunnel City group. Fu et al. (2015) determined that the glauconite at their study site had a higher aluminum to silicon ratio. Berthierine contains a lot of aluminum so to effectively sequester magnesium and iron the parent glauconite must have a similar aluminum to silicon ratio to be significant. Those models also assumed a lower temperature and a lower alkalinity. There might be further influence from reducing minerals like pyrite that can induce oxic waters to lose enough oxygen that they become under saturated with respect to glauconite. Experimental evidence suggests that glauconite is under saturated at experimental conditions and at saturation with dolomite and siderite supporting the claim that glauconite is able to sequester carbon.

Tables

Table 1. Physical evolution of the core

	Core Diameter (mm)	Core Length (mm)	Pre-experiment core mass (g)	Dissolved core mass (g)	Percent dissolved	Percent porosity post-experiment	Initial Permiability (m^2)	Final Permiability (m^2)
Exp. 1	12.5	26.2	5.841	0.147	2.52	15	– [a]	6.95×10^{-14}
Exp. 2	12.3	26.3	5.605	0.131	2.35	13	1.59×10^{-12}	1.03×10^{-13}

[a] (–) indicates that consistent pressure differential was not able to be measured so permeability was not determined

Table 2. Bulk composition of the sandstone in weight percent (wt%)

Al_2O_3	5.3
BaO	0.03
CaO	2.0
Fe_3O_2	8.6
FeO	1.9
K_2O	5.0
MgO	2.2
MnO	0.05
Na_2O	0.03
P_2O_5	0.2
SiO_2	69.1
SrO	0.005
TiO_2	0.1
Loss on ignition	5.2
Total	99.7

Table 3. Abundance of minerals in the core

	Mole Fraction	**Weight Percent**
Quartz	0.79	39
Glauconite	0.11	38
K-Feldspar	0.07	15
Dolomite	0.03	5
Siderite	0.02	2
Total	1	100

Table 4. Chemical composition of the glauconite in weight percent (wt%)

Al_2O_3	8.0
BaO	0.005
CaO	0.46
Fe_3O_2	21.4
FeO	1.3
K_2O	7.3
MgO	3.1
MnO	0.02
Na_2O	1.5
P_2O_5	0.062
SiO_2	50.1
SrO	0.002
TiO_2	0.08
Loss on ignition	6.4
Total	99.7

Table 5. Dissolved chemistry of fluids following reaction with glauconite bearing core at 150°C, 200 bars (confining pressure). Results from this experiment (experiment 1) provide data under non-reducing conditions, providing a reference for comparison with alteration processes recognized during experiment 2, which contained dissolved H_2 from an external redox buffer, which served as a reducing agent.

ml of sol through the core	**Time (hrs)**	**CO2 (mol/kg)** [a]	**Alk (meq/kg)** [b]	**Al^{3+} (umol/kg)**	**Ca^{2+} (mmol/kg)**	**Fe^{2+} (umol/kg)**	**K^{+} (mmol/kg)**	**Mg^{2+} (mmol/kg)**	**Na^{+} (mmol/kg)**	**SiO2 (mmol/kg)**
	pre	0.58	92						1030	
6	10-dil	0.15		<DL	9.2	17	8.2	5.7	749	1.02
6	10-corr		73	<DL	12.3	23	10.9	7.6	996	1.36
13	22.26	0.35	90	<DL	0.62	16	2.5	3.5	1003	2.06
27	45.97	0.42	85	<DL	0.98	14	1.82	1.05	1012	1.93
41	69.91	0.45	90	<DL	0.95	9	1.57	0.89	1001	1.57
128	213.81	0.47	86	<DL	0.45	11	0.96	0.3	1026	1.05
213	356.58	0.49	85	<DL	0.34	8	0.8	0.21	1042	0.93
301	502.08	0.50	83	<DL	0.32	16	0.72	0.15	1004	1.19
329	549.41	0.54	81	22	0.32	13	0.69	0.15	975	1.74
372	621.16	0.52	73	<DL	0.29	32	0.61	0.14	932	1.49
460	766.98	0.51	74	<DL	0.3	10	0.62	0.11	921	1.16

a. Determined using the manometric technique. b. Total alkalinity measured by gran titration. 2σ error for total alkalinity is 2 meq/kg.

Table 6. Dissolved chemistry of fluids following reaction with a glauconite bearing core at 150C, 200 bars in the presence of an external redox buffer. Results of experiment 2 elucidates the difference in species concentrations under oxic conditions (Table 5) and reducing conditions. Most important were increases in the concentration of iron and potassium in the brine post-interaction with the core.

ml of sol through the core	**Time(hrs)**	**H_2 (mmol/ kg)**	**CO_2 (mol/ kg)**	**Alk (meq/ kg)**	**Al^{3+} (umol/ kg)**	**Ca^{2+} (mmol/ kg)**	**Fe^{2+} (umol/ kg)**	**K^+ (mmol/ kg)**	**Mg^{2+} (mmol/ kg)**	**Na^+ (mmol/ kg)**	**SiO2 (mmol/ kg)**
	pre		0.56	98							
8	13.9	5		4	5	0.39	3	1.33	0.09	0.8	0.9
18	31-dil		0.20		<DL	2.73	38	3.84	2.34	796	1.8
18	31-corr	32		63	<DL	3.38	47	4.75	2.89	985	2.22
27	45.9	39	0.31	84	<DL	0.55	30	1.88	0.5	943	2.78
43	72.02	35	0.40	83	5	0.72	27	1.54	0.36	965	2.35
57	95.55	34	0.45	84	<DL	0.66	30	1.45	0.34	973	2.21
143	239.74	22	0.43	86	<DL	0.31	11	1.08	0.17	985	1.62
232	387.45	14	0.51	83	7	0.32	21	1.42	0.17	947	1.38
334	557.1	6	0.53	83	<DL	0.32	15	0.87	0.17	931	1.24

Table 7. Mossbauer spectra for samples of the glauconitic rock. The unreacted rock provides a baseline condition for the rock prior to alteration with the brine. Changes in the ferrous ferric ratio elucidate the alteration of glauconite to different minerals. Characteristic isomer shifts and quadrupole splitting allow for the characterization of the gain and loss of minerals like siderite.

Sample	Doublet Type	Isomer Shift (mm/s)	Quadrupole Splitting (mm/s)	Width (FWHM)	Area (Relative)	Ferrous /Ferric
Unreacted Rock	Ferric	0.364	0.486	0.572	0.832	0.24
	Ferrous	1.181	1.729	0.526	0.144	
	Ferrous	1.188	2.657	0.317	0.0548	
Experiment 1	Ferric	0.235	0.499	0.542	0.22	0.22
Upstream Region	Ferric	0.404	0.433	0.703	0.599	
	Ferrous	1.074	1.854	0.705	0.135	
	Ferrous	1.625	1.546	0.503	0.0436	
Experiment 2	Ferric	0.359	0.497	0.605	0.778	0.34
Upstream Region	Ferrous	1.217	1.78	0.566	0.229	
	Ferrous	1.19	2.673	0.302	0.0343	

Table 8. Extraction efficiency of selected elements for experiment 1. Integration of the fluid chemistry from experiment 1 shows preferential element removal relative to the abundance in the core. Calcium is the most mobile element suggesting that carbonates are being preferentially removed from the core. The difference in recovery rates between elements can suggest the formation of a secondary phases.

ml of sol through the core	**Time(hrs)**	**Ca recovery (wt %)**	**Fe recovery (wt %)**	**K recovery (wt %)**	**Mg recovery (wt %)**	**Si recovery (wt %)**
6	10-corr	3.5	0.0015	1.0	1.4	0.012
13	22.26	5.7	0.0029	1.6	2.7	0.030
27	45.97	6.2	0.0051	2.1	3.7	0.071
41	69.91	6.9	0.0069	2.4	4.1	0.107
128	213.81	9.7	0.0159	4.0	5.7	0.269
213	356.58	11.3	0.0245	5.0	6.3	0.391
301	502.08	12.7	0.0356	6.0	6.8	0.525
329	549.41	13.1	0.0398	6.3	6.9	0.585
372	621.16	13.7	0.0496	6.7	7.1	0.685
460	766.98	14.9	0.0684	7.4	7.5	0.852
464	774.12	14.9	0.0688	7.5	7.5	0.859

Table 9. Extraction efficiency of selected elements for experiment 2. Results show how the addition of a reducing agent affects the relative efflux of elements from the core. Differences in absolute magnitude are not indicative of the redox environment because they are due to different start protocols between the two experiments. Changes in relative magnitudes however are relevant.

ml of sol through the core	**Time(hrs)**	**Ca recovery (wt %)**	**Fe recovery (wt %)**	**K recovery (wt %)**	**Mg recovery (wt %)**	**Si recovery (wt %)**
8	13.9	0.2	0.0003	0.2	0.0	0.011
18	31-corr	0.9	0.0026	0.6	0.4	0.032
27	45.9	1.6	0.0058	0.9	0.8	0.063
43	72.02	2.1	0.0106	1.3	1.0	0.123
57	95.55	2.6	0.0149	1.6	1.2	0.171
143	239.74	4.6	0.0340	3.2	1.9	0.419
232	387.45	6.0	0.0496	4.9	2.4	0.618
334	557.1	7.6	0.0697	6.6	2.9	0.818
486	810.8	9.9	0.0952	8.5	3.8	1.10

Figures

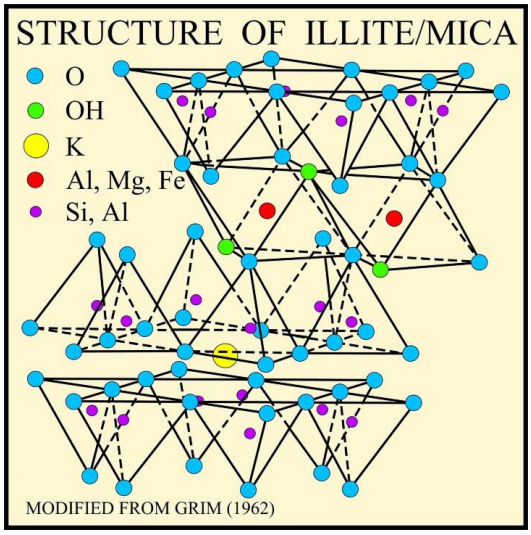

Figure 1. Glauconite is structurally similar to illite (Thompson and Hower 1975).

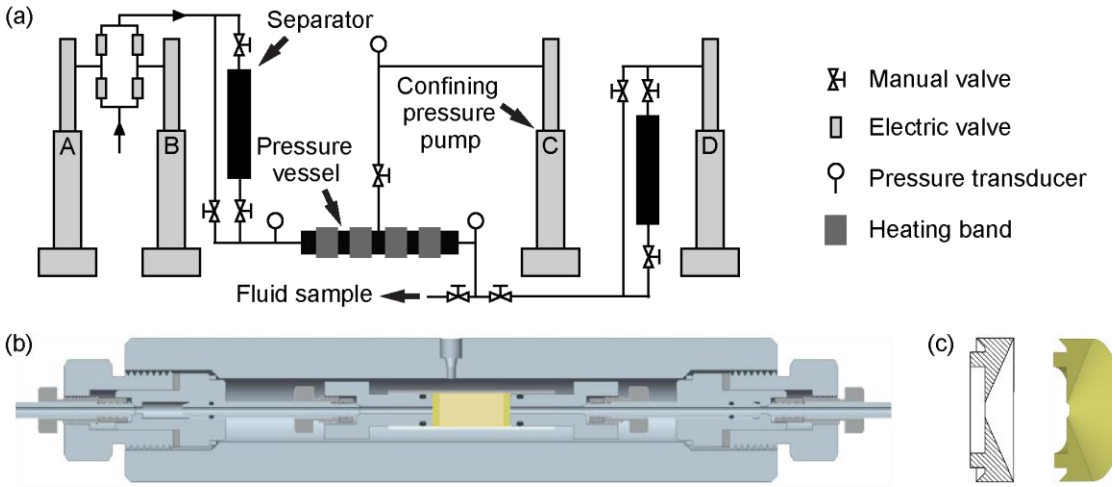

Figure 2. (a) Schematic for the flow reactor (b) Confining vessel assembled with titanium closure pieces and delivery line to the core (c) PEEK retainer ring, showing the conical shape that ensures that flow occurs through the entire cross section of the core. (Luhmann et al. 2013, 2014; Tutolo et al. 2014, 2015).

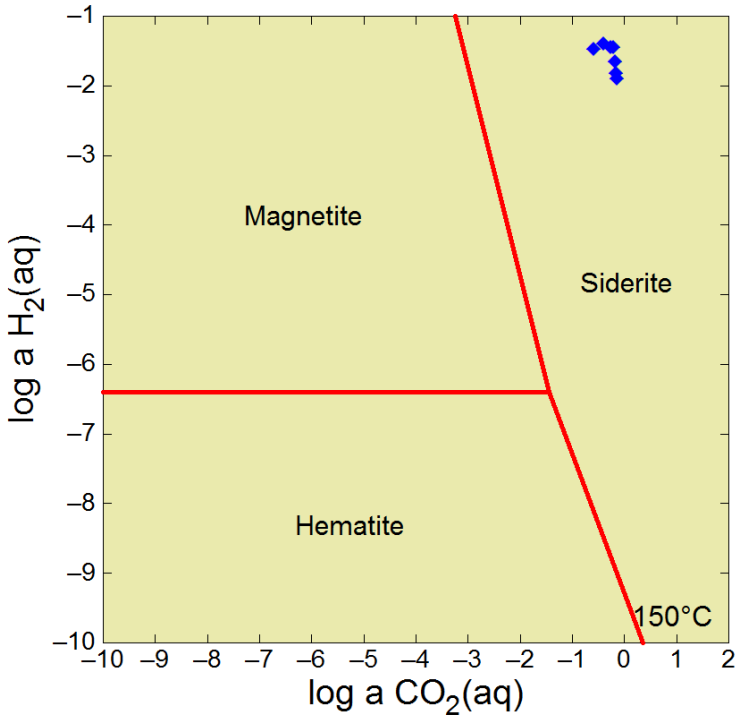

Figure 3. Dissolved gas data from experiment 2 plotted onto a stability diagram for iron minerals. The conditions suggest that the precipitation of siderite was highly favorable and that other iron minerals were unstable during experiment 2.

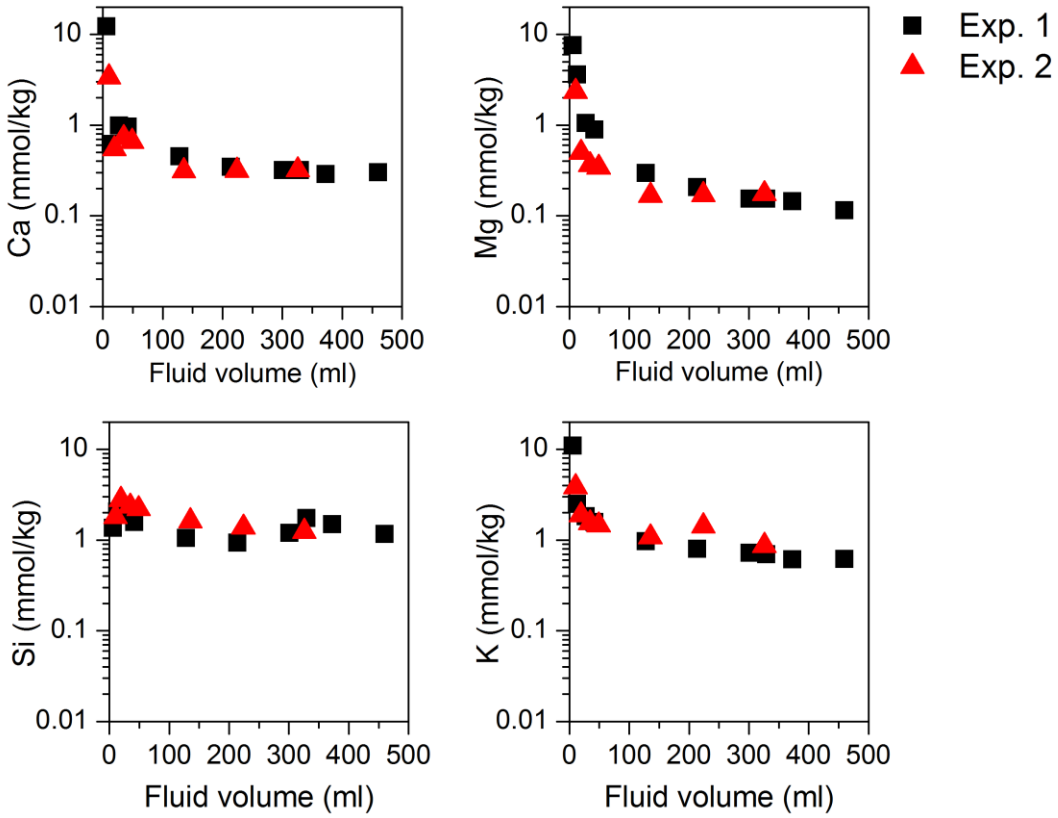

Figure 4. Outlet fluid chemistry for both experiments. The behavior of the pore fluid chemistry was similar for both experiments reaching roughly the same steady state values. Fluid chemistry shows and extremely fast rate of dissolution at the beginning of both experiments believe to be related to an early abundance of reactive sites in the minerals of the core. One important distinction between the two experiments is that during experiment 2 dissolved Mg appeared to reach steady state values faster.

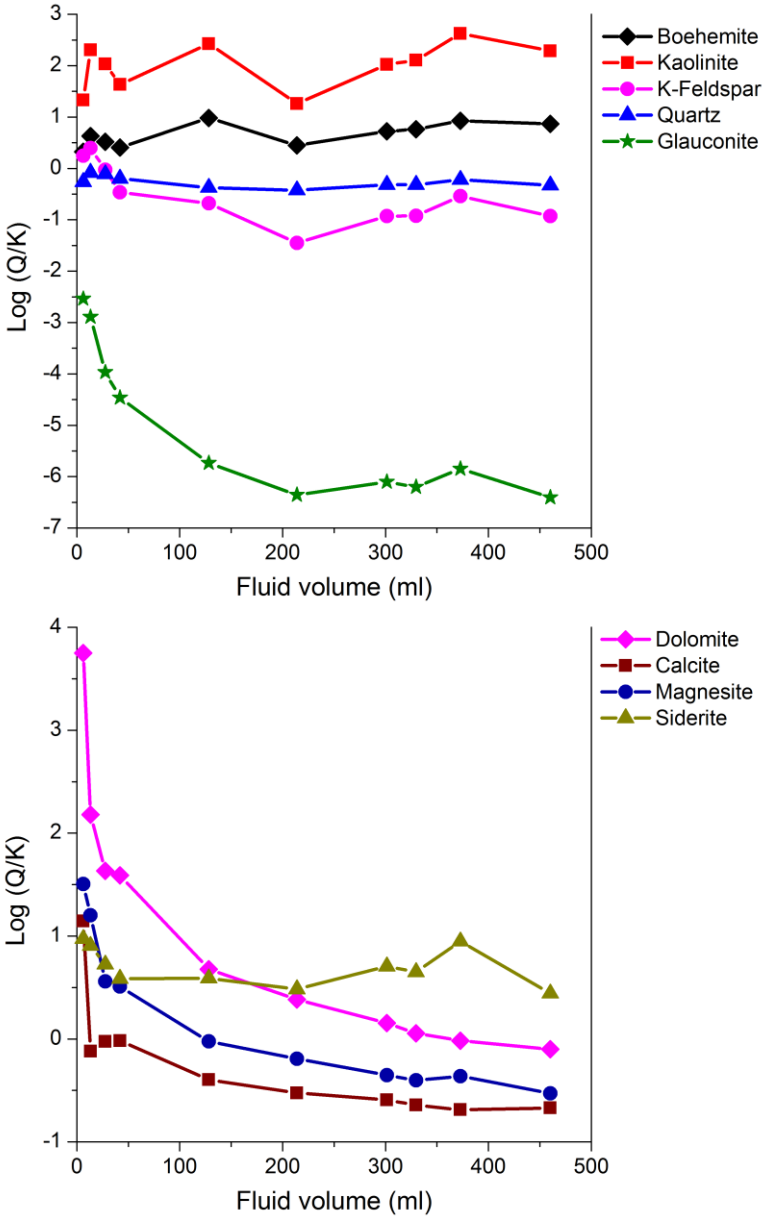

Figure 5. Saturation indices for experiment 1 under oxidizing conditions. Kaolinite was consistently the most oversaturated aluminum mineral in all of the calculations and was selected as a representative phase because it is a predicted weathering product in several geochemical models of carbon sequestration (Pham et al. 2011; Xu et al. 2004). Siderite and dolomite appear to be supersaturated for the entire length of the experiment. These results suggest that minerals like K-feldspar and glauconite were altered to clays and that carbonate minerals would be able to precipitate from the brine because of dissolved cations from the core.

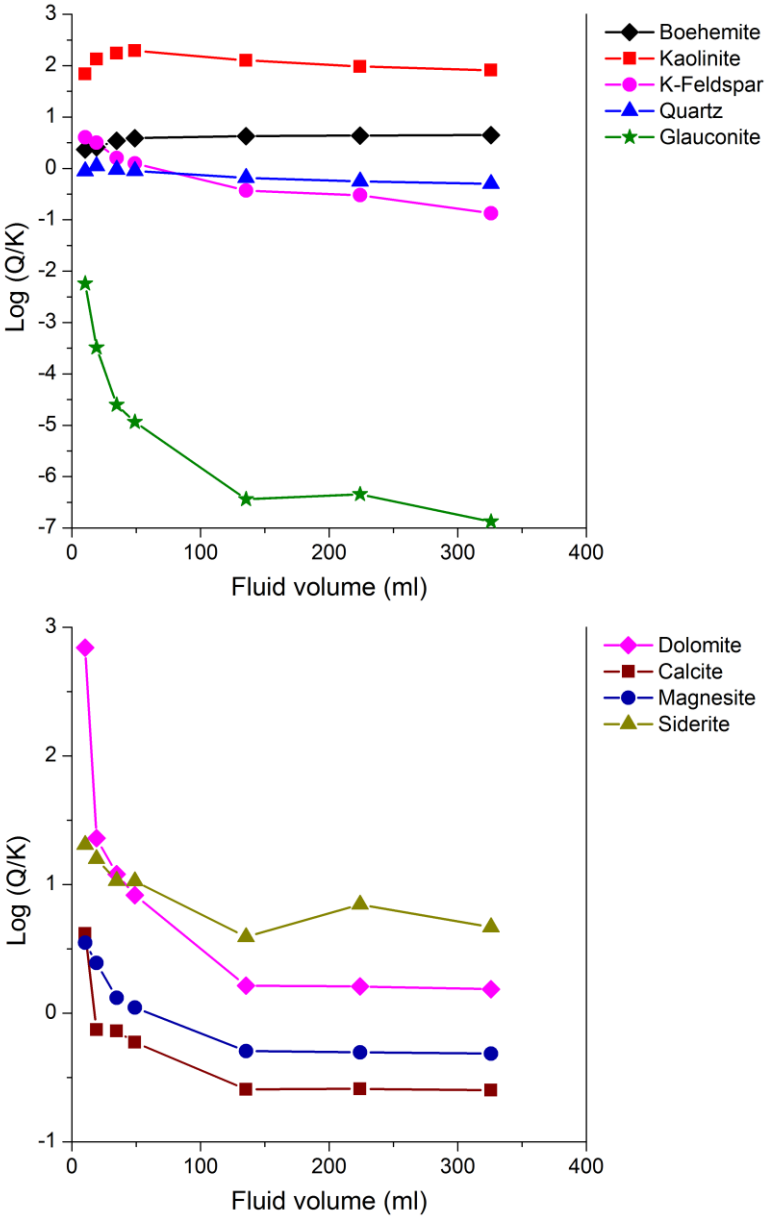

Figure 6. Saturation indices for experiment 2 which included a redox buffer. These indices were calculated using the measured values for the activity of CO_2 and H_2 and total alkalinity. The accuracy of these calculations is dependent on the sensitivity of instruments like pH probes to supply data for the equilibrium expression for carbonate precipitation. These results show the change is saturation with respect to siderite consistent with the different redox environment.

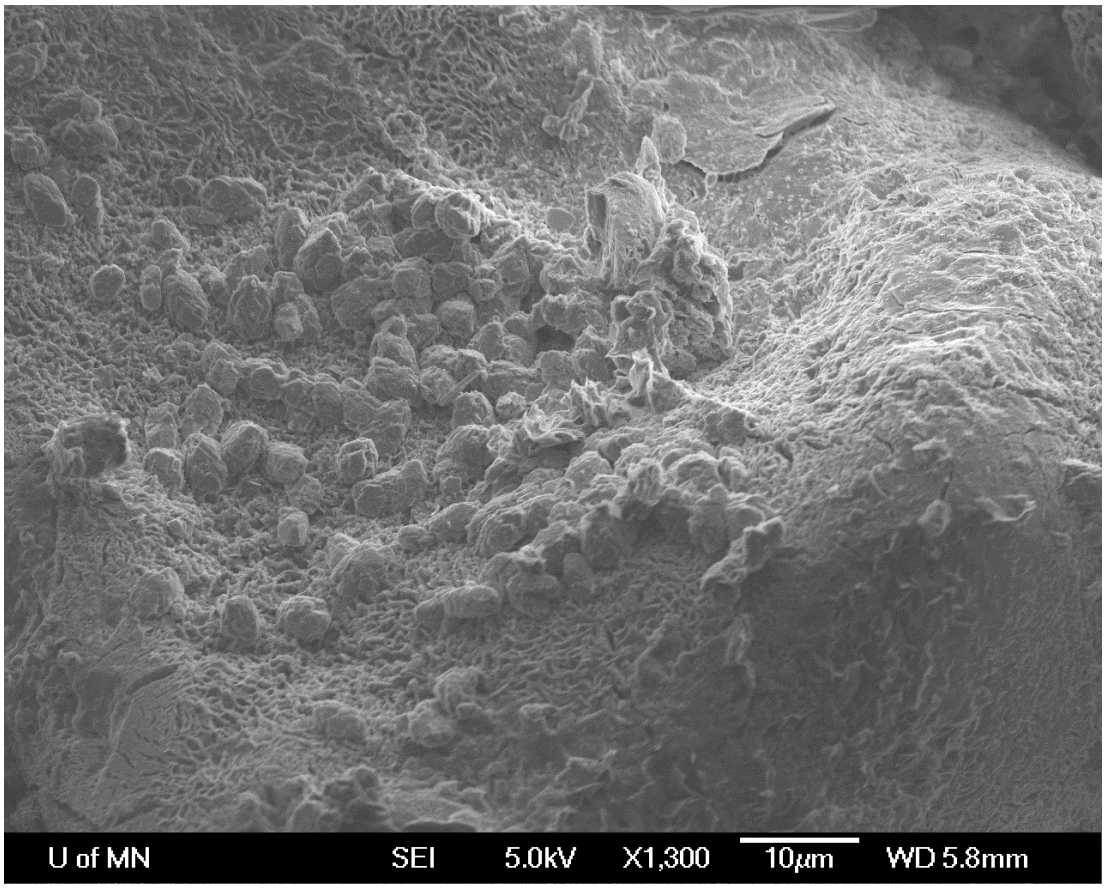

Figure 7. An altered glauconite grain from experiment 1. A small area of pristine mineral coating can be seen in the lower left part of the image adjacent to an alteration surface that is more honeycomb-like or micaceous. Alteration of the grain shows that glauconite is reactive during experiment 1. Botryoidal iron oxides can be seen in the center of the image.

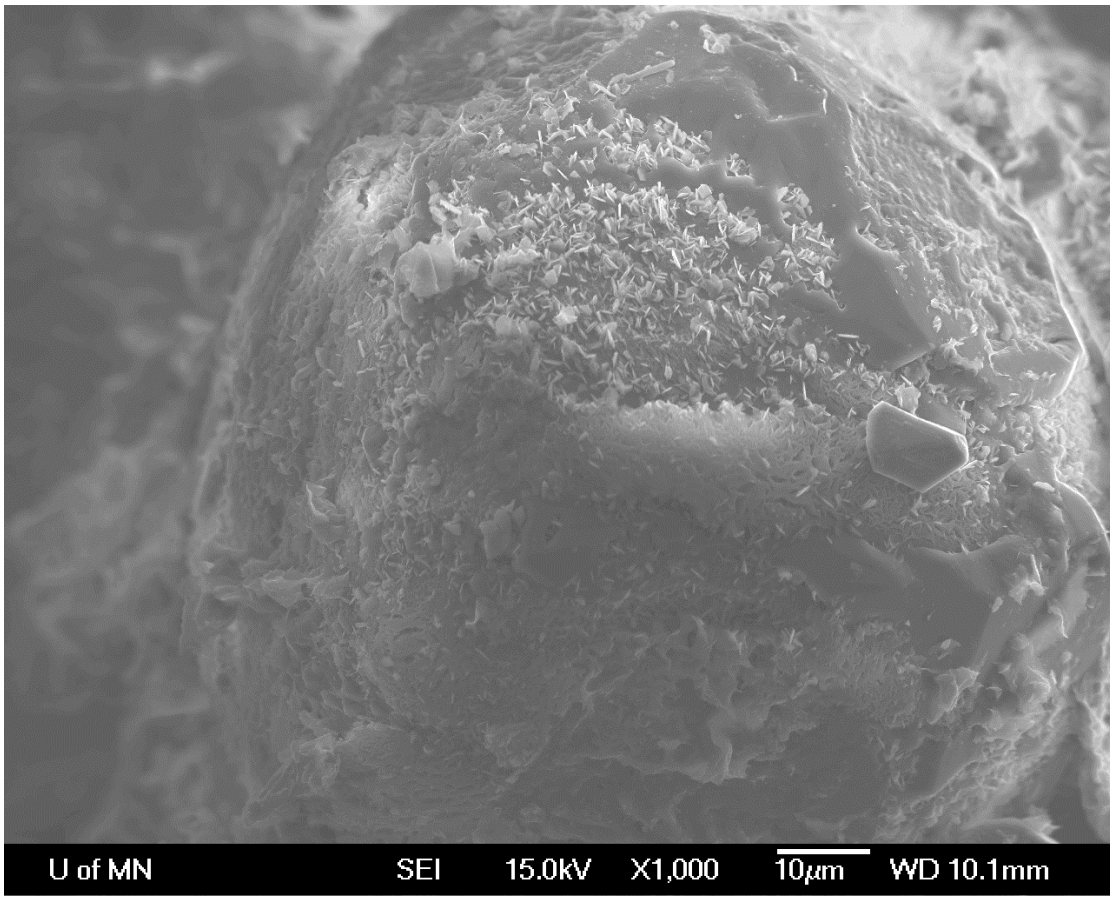

Figure 8. Secondary mineral precipitation during experiment 2. Platy aluminum bearing minerals were found on this quartz grain. This suggests mobilization of aluminum from glauconite (visible in the lower half of the image) to secondary phases like kaolinite and boehmite. These are the sheeted minerals that contribute to decrease in permeability and reactive surface area in the core.

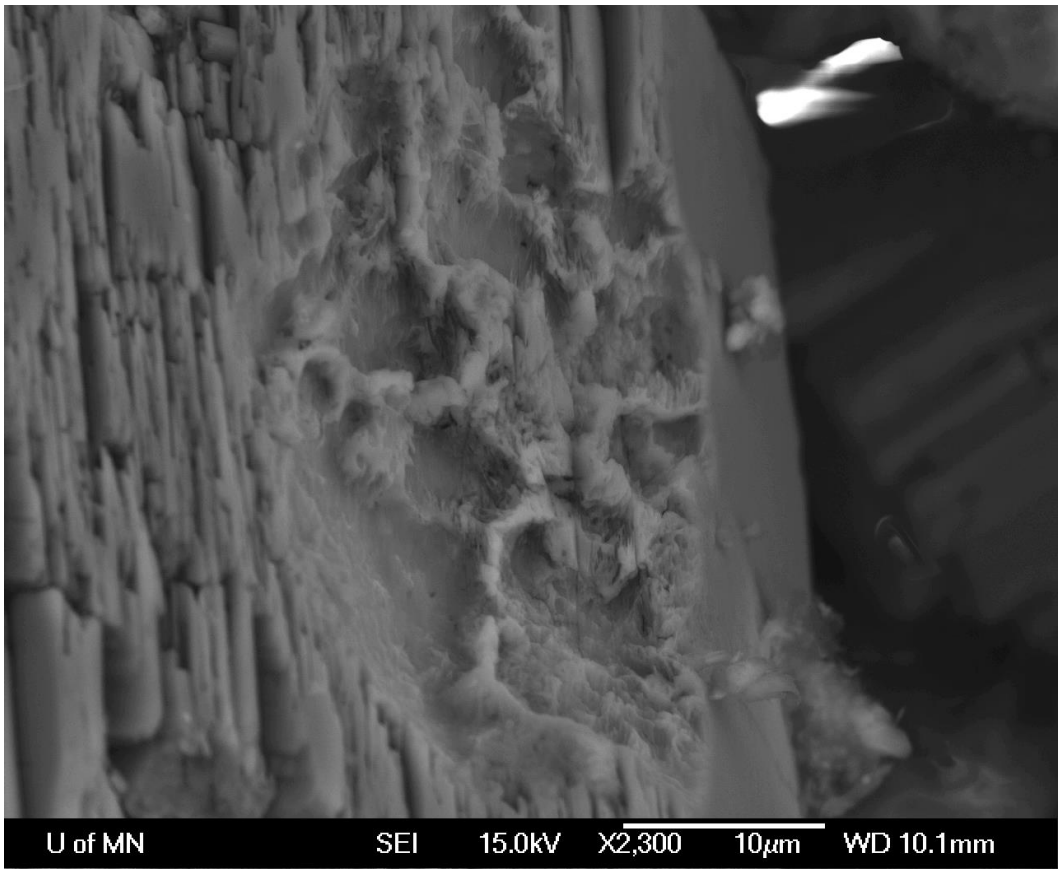

Figure 9. Dissolution of silicates during experiment 2. Etching of this feldspar grain is evident along with the formation of a wispy secondary phase. Dissolution of the grain is evidence of mass transfer from minerals to solution and alteration to clays shows the reduction of reactive surface area.

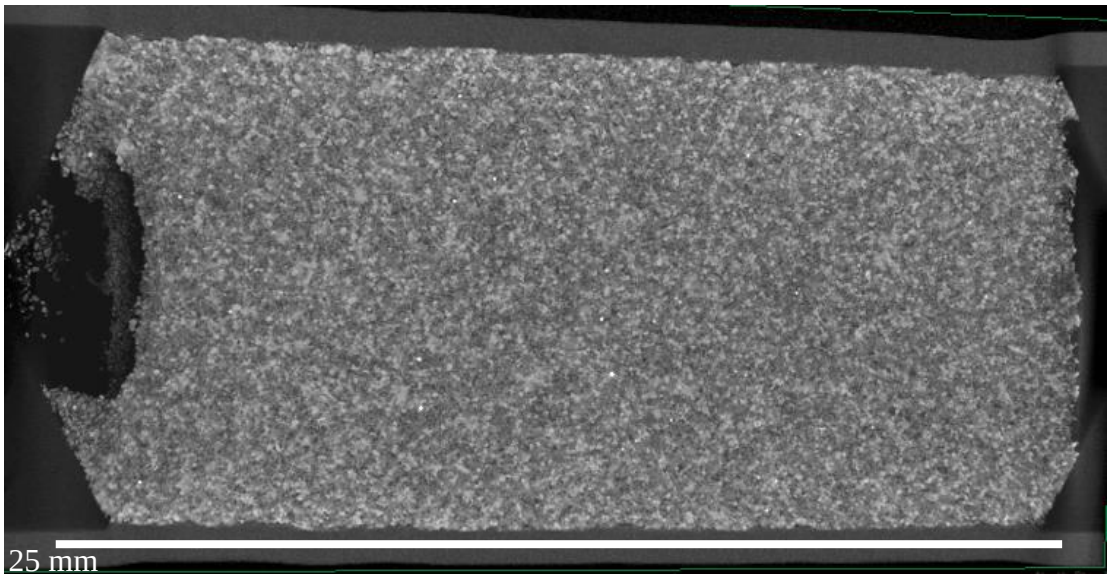

Figure 10. XRCT image of the first experimental core. Reaction with the brine appears to have caused grain reorganization on the upstream side of the core and physical compaction against the downstream side. The coarse grained sediment shows that the rock contains well-connected pores spaces.

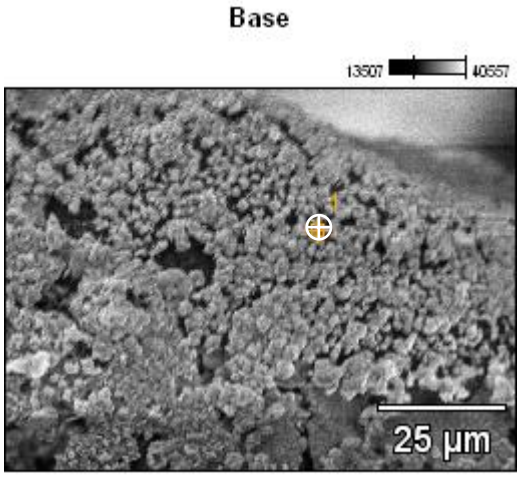

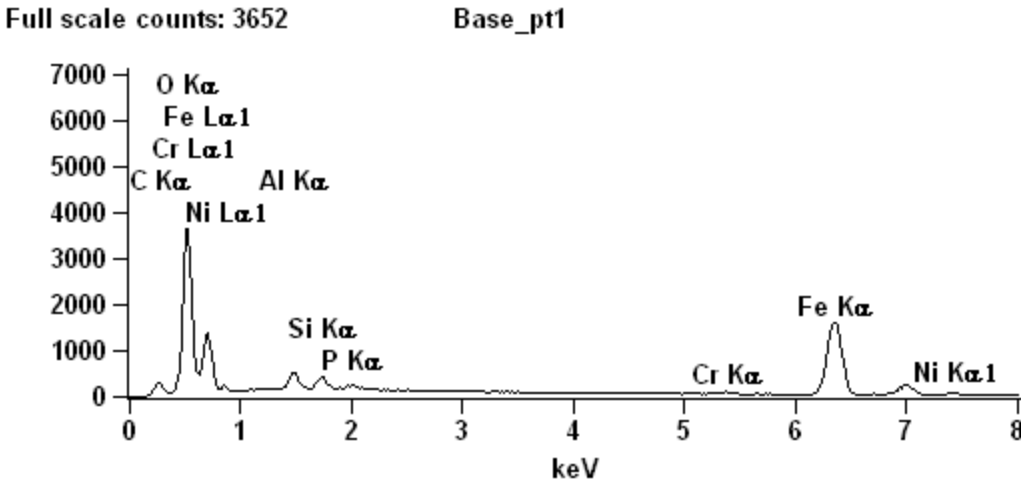

Atom %

	O	*Al*	*Si*	*P*	*Cr*	*Fe*	*Ni*
Point 1	63.8	2.3	1.5	0.5	0.3	30.9	0.7

Atom % Error

	O	*Al*	*Si*	*P*	*Cr*	*Fe*	*Ni*
Point 1	+/-2.07	+/-0.09	+/-0.09	+/-0.07	+/-0.04	+/-0.32	+/-0.12

Figure 11. X-ray dispersive spectroscopy of iron minerals from experiment 1. EDS allows for the iron minerals the precipitated during experiment 1 to be characterized. The iron to oxygen ratio and mineral habit is highly diagnostic of iron oxides. As secondary phases this analysis helps constrain the redox environment for experiment 1.

Bibliography

Aagaard P. and Helgeson H. C. (1982) Thermodynamic and kinetic constraints on reaction rates among minerals and aqueous solutions. I. Theoretical considerations. *Am. J. Sci.* **282**, 237–285.

Aagaard P., Oelkers E. H. and Schott J. (2004) Glauconite dissolution kinetics and application to CO_2 storage in the subsurface. *Geochim. Cosmochim. Acta* **68**, A143–A143.

Alekseyev V. A., Medvedeva L. S., Prisyagina N. I., Meshalkin S. S. and Balabin A. I. (1997) Change in the dissolution rates of alkali feldspars as a result of secondary mineral precipitation and approach to equilibrium. *Geochim. Cosmochim. Acta* **61**, 1125–1142.

Alexander S. C. and Saar M. O. (2012) Improved Characterization of Small "u" for Jacob Pumping Test Analysis Methods. *Ground Water* **50**, 256–265.

Barnes, I., & Clarke, F. E. (1969) Chemical properties of ground water and their corrosion and encrustation effects on wells. *Hydrology of aquifer systems*., 1–210

Brantley S. L., White A. F. and Kubicki J. D. (2008) *Kinetics of water-rock interaction*., Springer New York.

Butler I. B., Schoonen M. A. and Rickard D. T. (1994) Removal of dissolved oxygen from water: A comparison of four common techniques. *Talanta* **41**, 211–215.

Cerda C. M. (1987) Mobilization of kaolinite fines in porous media. *Colloids and Surfaces* **27**, 219–241.

Chafetz H. S. and Reid A. (2000) Syndepositional shallow-water precipitation of glauconitic minerals. *Sediment. Geol.* **136**, 29–42.

Courbe C., Velde B. and Meunier A. (1981) Weathering of glauconites: reversal of the glauconitization process in a soil profile in western France. *Clay Miner.* **16**, 231–243.

Curtis C. D. (1989) Green Marine Clays. Oolitic Ironstone Facies, Verdine Facies, Glaucony Facies and Celadonite-Bearing Facies — A Comparative Study. *Clay Miner.* **24**, 565–566.

Deer, W.A., Howie, R.A. and Zussman, J. (1962) Glauconite, in *Rock Forming Minerals*,

Sheet Silicates **3**, 35-41

DePaolo D. J. and Cole D. R. (2013) Geochemistry of Geologic Carbon Sequestration: An Overview. *Rev. Mineral. Geochemistry* **77**, 1–14.

Dove P. M. and Crerar D. A. (1990) Kinetics of quartz dissolution in electrolyte solutions using a hydrothermal mixed flow reactor. *Geochim. Cosmochim. Acta* **54**, 955–969.

Duan Z. and Sun R. (2003) An improved model calculating CO 2 solubility in pure water and aqueous NaCl solutions from 273 to 533 K and from 0 to 2000 bar. *Chem. Geol.* **193**, 257–271.

Duckworth O. W. and Martin S. T. (2004) Role of molecular oxygen in the dissolution of siderite and rhodochrosite1. *Geochim. Cosmochim. Acta* **68**, 607–621.

Dyar M. D., Agresti D. G., Schaefer M. W., Grant C. A. and Sklute E. C. (2006) Mössbauer Spectroscopy of Earth and Planetary Materials. *Annu. Rev. Earth Planet. Sci.* **34**, 83–125.

Dyar M. D., Schaefer M. W., Sklute E. C. and Bishop J. L. (2008) Mössbauer spectroscopy of phyllosilicates: effects of fitting models on recoil-free fractions and redox ratios. *Clay Miner.* **43**, 3–33.

Fanning D. S. (1989) Oxidation State of Iron in Glauconite from Oxidized and Reduced Zones of Soil-Geologic Columns1. *Clays Clay Miner.* **37**, 59–64.

Foustoukos D. I., Houghton J. L., Seyfried W. E., Sievert S. M. and Cody G. D. (2011) Kinetics of H_2-O_2-H_2O redox equilibria and formation of metastable H_2O_2 under low temperature hydrothermal conditions. *Geochim. Cosmochim. Acta* **75**, 1594–1607.

Fu Q., Lu P., Konishi H., Dilmore R., Xu H., Seyfried W. E. and Zhu C. (2009) Coupled alkali-feldspar dissolution and secondary mineral precipitation in batch systems: 1. New experiments at 200°C and 300bars. *Chem. Geol.* **258**, 125–135.

Fu Y., van Berk W., Schulz H.-M. and Mu N. (2015a) Berthierine formation in reservoir rocks from the Siri oilfield (Danish North Sea) as result of fluid–rock interactions: Part II. Deciphering organic–inorganic processes by hydrogeochemical modeling. *Mar. Pet. Geol.* **65**, 317–326.

Fu Y., van Berk W., Schulz H.-M. and Mu N. (2015b) Berthierine formation in reservoir rocks from the Siri oilfield (Danish North Sea) as result of fluid–rock interactions: Part III. Determining mineral stability and CO_2-sequestering capacity of glauconitic sandstones. *Mar. Pet. Geol.* **65**, 327–333.

Garrels R. M. (1965) Silica: Role in the Buffering of Natural Waters. *Science* **148**, 69.

Garrels R. M. and Mackenzie F. T. (1967) Origin of the chemical composition of some springs and lakes. In *Equilibrium Concepts in Natural Water Systems* (ed. W. Stumm). W.W. Norton. pp. 222–242.

Gilfillan S. M. V, Lollar B. S., Holland G., Blagburn D., Stevens S., Schoell M., Cassidy M., Ding Z., Zhou Z., Lacrampe-Couloume G. and Ballentine C. J. (2009) Solubility trapping in formation water as dominant CO(2) sink in natural gas fields. *Nature* **458**, 614–618.

Golubev S. V., Bénézeth P., Schott J., Dandurand J. L. and Castillo A. (2009) Siderite dissolution kinetics in acidic aqueous solutions from 25 to 100 °C and 0 to 50 atm pCO_2. *Chem. Geol.* **260**, 295–301.

Gran G., Dahlenborg H., Laurell S. and Rottenberg M. (1950) Determination of the Equivalent Point in Potentiometric Titrations. *Acta Chem. Scand.* **4**, 559–577.

Gunter W. D., Wiwchar B. and Perkins E. H. (1997) Aquifer disposal of CO_2-rich Greenhouse Gases: Extension of the time scale of experiment for CO_2-sequestering reactions by geochemical modelling. *Mineral. Petrol.* **59**, 121–140.

Hassan M. S. and Baioumy H. M. (2006) Structural and chemical alteration of glauconite under progressive acid treatment. *Clays Clay Miner.* **54**, 491–499.

Helgeson H. C., Delany J. M., Nesbitt H. W. and Bird D. K. (1978) Summary and Critique of the Thermodynamic Properties of Rock-Forming Minerals. *Am J Sci* **278 -A**.

Helgeson H. C., Murphy W. M. and Aagaard P. (1984) Thermodynamic and kinetic constraints on reaction rates among minerals and aqueous solutions. II. Rate constants, effective surface area, and the hydrolysis of feldspar. *Geochim. Cosmochim. Acta* **48**, 2405–2432.

Hellevang H., Pham V. T. H. and Aagaard P. (2013) Kinetic modelling of CO_2-water-rock interactions. *Int. J. Greenh. Gas Control* **15**, 3–15.

Hellmann R. (1994) The albite-water system: Part I. The kinetics of dissolution as a function of pH at 100, 200 and 300°C. *Geochim. Cosmochim. Acta* **58**, 595–611.

Hem J. D. (1960) Restraints on dissolved ferrous iron imposed by bicarbonate redox potential, and pH. *U. S. Geol. Surv. Water-Supply Pap.*

Hutcheon I. and Abercrombie H. (1990) Carbon dioxide in clastic rocks and silicate hydrolysis. *Geology* **18**, 541–544.

Hutcheon I., Shevalier M. and Abercrombie H. J. (1993) pH buffering by metastable mineral-fluid equilibria and evolution of carbon dioxide fugacity during burial diagenesis. *Geochim. Cosmochim. Acta* **57**, 1017–1027.

IPCC (2005) *IPCC special report on carbon dioxide capture and storage*.,

Jensen D. L., Boddum J. K., Tjell J. C. and Christensen T. H. (2002) The solubility of rhodochrosite (MnCO3) and siderite (FeCO3) in anaerobic aquatic environments. *Appl. Geochemistry* **17**, 503–511.

Johnson J. W., Oelkers E. H. and Helgeson H. C. (1992) SUPCRT92: A software package for calculating the standard molal thermodynamic properties of minerals, gases, aqueous species, and reactions from 1 to 5000 bar and 0 to 1000°C. *Comput. Geosci.* **18**, 899–947.

Kaszuba J. P., Janecky D. R. and Snow M. G. (2003) Carbon dioxide reaction processes in a model brine aquifer at 200°C and 200 bars: Implications for geologic sequestration of carbon. *Appl. Geochemistry* **18**, 1065–1080.

Kaszuba J. P., Janecky D. R. and Snow M. G. (2005) Experimental evaluation of mixed fluid reactions between supercritical carbon dioxide and NaCl brine: Relevance to the integrity of a geologic carbon repository. *Chem. Geol.* **217**, 277–293.

Kelemen P. and Matter J. (2008) In situ carbonation of peridotite for CO_2 storage. *Proc. Natl. Acad. Sci. U. S. A.* **105**, 17295–17300.

Kharaka Y. and Hanor J. (2007) Deep fluids in the continents: I. Sedimentary basins. In *Treatise on geochemistry* pp. 1–48.

Kong X. Z., Tutolo B. M. and Saar M. O. (2013) DBCreate: A SUPCRT92-based program for producing EQ3/6, TOUGHREACT, and GWB thermodynamic databases at user-defined T and P. *Comput. Geosci.* **51**, 415–417.

Kumar A., Noh M., Pope G. A., Sepehrnoori K., Bryant S. and Lake L. W. (2004) Reservoir Simulation of CO_2 Storage in Deep Saline Aquifers. *SPE/DOE Symp. Improv. Oil Recover.*

Lindberg R. D. and Runnells D. D. (1984) Ground water redox reactions: an analysis of equilibrium state applied to eh measurements and geochemical modeling. *Science* **225**, 925–927.

Linstrom P. J. and Mallard W. G. (2000) *NIST Chemistry WebBook, NIST Standard Reference Database Number 69*., National Institute of Standards and Technology.

Lu P., Fu Q., Seyfried W. E., Hedges S. W., Soong Y., Jones K. and Zhu C. (2013) Coupled alkali feldspar dissolution and secondary mineral precipitation in batch systems - 2: New experiments with supercritical CO_2 and implications for carbon sequestration. *Appl. Geochemistry* **30**, 75–90.

Luhmann A. J., Kong X. Z., Tutolo B. M., Ding K., Saar M. O. and Seyfried W. E. (2013) Permeability reduction produced by grain reorganization and accumulation of exsolved CO_2 during geologic carbon sequestration: A new CO_2 trapping mechanism. *Environ. Sci. Technol.* **47**, 242–251.

Luhmann A. J., Kong X. Z., Tutolo B. M., Garapati N., Bagley B. C., Saar M. O. and Seyfried W. E. (2014) Experimental dissolution of dolomite by CO_2-charged brine at 100°C and 150bar: Evolution of porosity, permeability, and reactive surface area. *Chem. Geol.* **380**, 145–160.

Luquot L., Andreani M., Gouze P. and Camps P. (2012) CO_2 percolation experiment through chlorite/zeolite-rich sandstone (Pretty Hill Formation – Otway Basin–Australia). *Chem. Geol.* **294-295**, 75–88.

Otake T., Wesolowski D. J., Anovitz L. M., Allard L. F. and Ohmoto H. (2007) Experimental evidence for non-redox transformations between magnetite and hematite under H2-rich hydrothermal conditions. *Earth Planet. Sci. Lett.* **257**, 60–70.

Otake T., Wesolowski D. J., Anovitz L. M., Allard L. F. and Ohmoto H. (2010) Mechanisms of iron oxide transformations in hydrothermal systems. *Geochim. Cosmochim. Acta* **74**, 6141–6156.

Palandri J. L. and Kharaka Y. K. (2004) A compilation of rate parameters of water-mineral interaction kinetics for application to geochemical modeling. *U.S. Geol. Surv. Open file Rep.* **2004-1068**, 71.

Palandri J. L., Rosenbauer R. J. and Kharaka Y. K. (2005) Ferric iron in sediments as a novel CO_2 mineral trap: CO_2-SO_2 reaction with hematite. *Appl. Geochemistry* **20**, 2038–2048.

Pentland C. H., El-Maghraby R., Georgiadis A., Iglauer S. and Blunt M. J. (2011) Immiscible displacements and capillary trapping in CO_2 storage. In *Energy Procedia* pp. 4969–4976.

Pham V. T. H., Lu P., Aagaard P., Zhu C. and Hellevang H. (2011) On the potential of CO_2-water-rock interactions for CO_2 storage using a modified kinetic model. *Int. J. Greenh. Gas Control* **5**, 1002–1015.

Pokrovsky O. S., Golubev S. V. and Schott J. (2005) Dissolution kinetics of calcite, dolomite and magnesite at 25 °C and 0 to 50 atm pCO_2. *Chem. Geol.* **217**, 239–255.

Saldi G. D., Jordan G., Schott J. and Oelkers E. H. (2009) Magnesite growth rates as a function of temperature and saturation state. *Geochim. Cosmochim. Acta* **73**, 5646–5657.

Sass, B. M., Gupta, N., Ickes, J. A., Engelhard, M. H., Baer, D. R., Bergman, P., & Byrer C. (2001) Interaction of rock minerals with carbon dioxide and brine: a hydrothermal investigation. *First Natl. Conf. Carbon Sequestration* **17**.

Seewald J. S. (1994) Evidence for metastable equilibrium between hydrocarbons under hydrothermal conditions. *Nature* **370**, 285–287.

Solomon S., Plattner G.-K., Knutti R. and Friedlingstein P. (2009) Irreversible climate change due to carbon dioxide emissions. *Proc. Natl. Acad. Sci. U. S. A.* **106**, 1704–1709.

Stefánsson A. (2001) Dissolution of primary minerals of basalt in natural waters I. Calculation of mineral solubilities from 0°C to 350°C. *Chem. Geol.* **172**, 225–250.

Sverjensky D. A., Shock E. L. and Helgeson H. C. (1997) Prediction of the thermodynamic properties of aqueous metal complexes to 1000 degrees C and 5 kb. *Geochim. Cosmochim. Acta* **61**, 1359–1412.

Tagirov B. and Schott J. (2001) Aluminum speciation in crustal fluids revisited. *Geochim. Cosmochim. Acta* **65**, 3965–3990.

Tardy Y., Duplay J. and Fritz B. (1987) Stability fields of smectites and illities as a function of temperature and chemical composition. *Proc. Int. Meet. Geochemistry Earth Surf. Process. Miner. Form.*, 461–494.

Tremaine P. R. and LeBlanc J. C. (1980) The solubility of magnetite and the hydrolysis and oxidation of Fe^{2+} in water to 300°C. *J. Solution Chem.* **9**, 415–442.

Tutolo B. M., Kong X. Z., Seyfried W. E. and Saar M. O. (2014) Internal consistency in aqueous geochemical data revisited: Applications to the aluminum system. *Geochim. Cosmochim. Acta* **133**, 216–234.

White A. F. and Brantley S. L. (1995) Chemical weathering rates of silicate minerals: An overview. In *Reviews in Mineralogy 31* Mineralogical Soc America. pp. 1–22.

White A. F. and Peterson M. L. (1990) Role of Reactive-Surface-Area Characterization in Geochemical Kinetic Models. In *Chemical Modeling of Aqueous Systems II* (eds. D. C. Melchior and R. L. Bassett). ACS Symposium Series. American Chemical Society. pp. 461–475.

Xu T., Apps J. A. and Pruess K. (2004) Numerical simulation of CO_2 disposal by mineral trapping in deep aquifers. *Appl. Geochemistry* **19**, 917–936.

Yang L. and Steefel C. I. (2008) Kaolinite dissolution and precipitation kinetics at 22 °C and pH 4. *Geochim. Cosmochim. Acta* **72**, 99–116.

Zhang L., Soong Y., Dilmore R. and Lopano C. (2015) Numerical simulation of porosity and permeability evolution of Mount Simon sandstone under geological carbon sequestration conditions. *Chem. Geol.* **403**, 1–12.

Appendix

Estimation of the molar volume of glauconite

Xu et al. (2004) calculated the molar volume of glauconite with a composition of $K_{1.5}Fe(III)_{2.5}Mg_{0.5}Fe(II)_{0.5}Al_1Si_{7.5}O_{20}(OH)_4$, as 284 cm^3/mol using crystallographic data from Deer et al. (1962) regarding the dimensions of a monoclinic cell. Notably, this glauconite stoichiometric formula is normalized to 20 $O(OH)_4$/mol glauconite unit cell. As noted above, Tardy et al. (1987) utilize a 10 $O(OH)_2$/mol glauconite unit cell normalization for their presented composition and we have chosen to employ that value here. Therefore, because the stoichiometric composition of our chosen glauconite is approximately half of the one presented by Xu et al. (2004) on a unit cell basis, we estimate that its volume should also be half of their presented volume or 142 cm^3/mol.

Determination of the third law entropy

Helgeson et al. (1978) states that the entropy of an unknown mineral can be estimated by writing a reversible reaction to known minerals of the same structural class. The entropy is related to these known minerals according to the following equasion:

$$S°_{i,Pr,Tr} = \frac{S°_{s,i,Pr,Tr}\left(V°_{s,i,Pr,Tr} + V°_{i,Pr,Tr}\right)}{2V°_{s,i,Pr,Tr}} \quad (8)$$

$S°$ is the third law entropy at standard temperature and pressure, $V°$ is the molar volume. The subscript *i* in eq. 6 means the thermodynamic property of the mineral of interest while the subscript *s* denotes "the sum of the [property] of the unknown mineral and the change in [the property] for the reaction (ΔS°r or ΔV°r)" (Helgeson et al. 1978). These unknown values are equal to the sum of the entropies and molar volumes of the known

minerals used in the hypothetical reversible reaction. Xu et al. suggested certain minerals to model this equation for glauconite and the elemental abundances were subsequently adjusted for our purposes (2004):

$$\text{glauconite} + \Delta S°r = 0.265\ K_2O + 0.021\ \text{greenalite} + 0.509\ \text{hematite} + 0.3367\ \text{talc} + 0.32\ \text{K-feldspar} + 1.37\ \text{quartz} + H_2O \quad (9)$$

Greenalite, K-feldspar and talc were chosen because they are representative of the coordination of the various metals in the structure of glauconite and they all have a monoclinic crystal symmetry. The thermodynamic data for the minerals with the exception of glauconite were taken from the SPRONS96.DAT file of SUPCRT92 (Johnson et al. 1992). The third law entropy for glauconite ($S°_{i,Pr,Tr}$) was determined to be 75.6 cal/(mol*K)

Determination of the Maier-Kelley heat capacity Coefficients

The heat capacity of glauconite was estimated by summing the heat capacities of its component oxides multiplied by their respective stoichiometric coefficient (Table A1).

Determination of the $\Delta G°_f$ of Glauconite

The $\Delta G°$ of the stoichiometric dissolution reaction was given by using the provided equilibrium constant for the solubility product in the following equation:

$$\Delta G° = -RT\ln K \quad (10)$$

$$\Delta G° = \sum \Delta G°f_{products} - \sum \Delta G°f_{reactants} \quad (11)$$

where *K* is the equilibrium constant for a given reaction, *T* is the temperature in Kelvin, *R* is the molar gas constant and $\Delta G°$ is Gibbs free energy of reaction. The ΔG° of formation of glauconite may be estimated per equation 7 by adding the sum of the Gibb's free energy for the product species to the Gibb's free energy of the reaction.

Using the thermodynamic parameters in SUPCRT

The SUPCRT92 (Johnson et al. 1992) program estimates the $\Delta G°_{P,T}$ of compounds using the Gibbs free energy equation where the heat capacity of the compound is substituted with the Maier-Kelley equation:

$$\Delta_a G°_{T,i} = \Delta_f G°_{Tr,i} - S°_{Tr,i}(T - T_r) + a_i \left[T - T_r - T \ln\left(\frac{T}{T_r}\right)\right] + (b_i/2)(2TT_r - T^2 - T_r^2) + (c_i(T^2 + T_r^2 - 2TT_r)/2TT_r^2) \quad (12)$$

Where *a*, *b* and *c* are the Maier-Kelley heat capacity coefficients of a mineral, $S°_{Tr,i}$ is the third law entropy for the mineral at standard temperature. *Tr* is the reference temperature, *T* denotes the temperature at which the unknown Gibb's free energy that is being estimated. The results for this calculation of the stoichiometric dissolution of glauconite for selected temperatures is shown in Table A3.

Table A1. Maier-Kelley heat capacity Coefficients for selected oxides

	stoichiometric coefficient	**a**	**b**	**c**
K_2O	0.425	18.51	8.65	-0.88
Fe_2O_3	0.515	23.49	18.6	-3.55
MgO	1.01	10.18	1.74	-1.48
Al_2O_3	0.16	21.742	11.065	-5.365
FeO	0.05	12.122	2.072	-0.75
SiO_2	3.73	11.22	8.2	-2.7
H_2O	1	7.1	8.24	0
Glauconite	1	83.28	55.71	-14.66

Table A2. Thermodynamic values used in the Gibb's free energy calculations

Log K_{sp} = 8.033 (Pham et al. 2011)

$\Delta G°$ = -10959 cal/mol

$\Delta G°_{f}$ reactants = -1380992 cal/mol

$\Delta G°_{f\ H2O}$ = -166624 cal/mol

$\Delta G°_{f\ Glauconite}$ = -1203409 cal/mol

Table A3. Solubility product of Glauconite at selected temperatures

Temp(°C)	Log Ksp
25	8.2191
50	6.4666
75	4.9135
100	3.5588
125	2.3736
150	1.3245
200	-0.4843